Article:

Zongyou, Z., Nimmo, W., Cai, C. et al. (2026) Ultra-low-cut-in galloping of a reverse-C-with-tail piezoelectric harvester for low-speed wind energy conversion. Sustainable Energy Technologies and Assessments, 92. 105244. ISSN: 2213-1388

https://doi.org/10.1016/j.seta.2026.105244

Ultra-Low-Cut-In Galloping of a Reverse-C-with-Tail Piezoelectric Harvester for Low-Speed Wind Energy Conversion

Zuo Zongyou[a,b,*], William Nimmo[b], Chang Cai[a], Qingan Li[a], Ning Jia[a], Xiangyu Sun[a,*]

[a] National Energy Wind Turbine Blade R&D Center, Institute of Engineering Thermophysics, Chinese Academy of Sciences, Beijing 100190, China

[b] University of Sheffield, Sheffield S10 2GD, United Kingdom

[*] Corresponding authors: Zongyou Zuo, Email: zuozongyou@iet.cn. Xiangyu Sun, Email: sunxiangyu@iet.cn

These authors contributed equally as co-corresponding authors.

Abstract

Galloping-based piezoelectric harvesters are promising for weak-wind energy conversion, but many existing designs still require a relatively high cut-in wind speed. This study proposes a reverse-C-with-tail bluff-body harvester to address this limitation. Preliminary fixed-body CFD results show stronger lift-coefficient fluctuations for the tailed geometry, while the pressure contours and streamlines qualitatively suggest a more extended recirculating-flow pattern and a more pronounced upper–lower pressure contrast. Wind tunnel experiments show a repeatable voltage-response-based cut-in at approximately 1 m/s. As the wind speed increases, the response becomes galloping-dominated. The S5 configuration reaches 46.4 V and a fixed-load power output of 2.152 mW at 7 m/s under R_L=1 MΩ, outperforming the tailless baseline. Further tests indicate that tail length is the primary geometric factor governing the reduction in the voltage-response-based cut-in wind speed and the subsequent output growth, while curved-section thickness provides secondary refinement. After A_1 and A_3 were fitted to the measured RMS-voltage data, the reduced-order electromechanical model reproduced the main voltage trends and provided an interpretive framework for the geometry-dependent response. These results establish the proposed configuration as an ultra-low-cut-in design strategy for galloping-based piezoelectric energy harvesting.

Keywords: Galloping-based energy harvesting; Piezoelectric harvester; Modified bluff body; Flow-induced vibration; Low wind speed; Ultra-low cut-in wind speed

1. Introduction

Vibration is a common ambient energy source in vehicles, ships, industrial machinery and other mechanical systems [1], [2]. Vibration energy harvesting (VEH) has therefore been widely investigated for powering low-consumption electronics, wireless sensors and distributed monitoring devices [3], [4], [5]. Among common VEH transduction mechanisms—electromagnetic [6], [7], [8], electrostatic [9], [10], and piezoelectric [11], [12], piezoelectric energy harvesting has received particular attention because of its compact structure, relatively high voltage output, and strong suitability for small-scale systems [13], [14], [15]. In flow-induced energy harvesting, several vibration mechanisms have been explored, including vortex-induced vibration [16], [17], [18], [19], [20], galloping [21], [22], [23], flutter [24], [25], [26], and buffeting [27], [28]. Galloping-based harvesters are especially attractive because, once triggered, they can generate large oscillation amplitudes and maintain an effective response over a relatively broad wind-speed range [29].

A common route to improve galloping-based piezoelectric wind energy harvesters is to modify the bluff-body geometry or the surrounding flow-control arrangement. Conventional studies have used square, triangular, D-shaped and other non-circular bluff bodies to generate negative aerodynamic damping and large transverse oscillations after galloping is established [30], [31], [32], [33]. More recent work has introduced curved plates, funnel-shaped sections, V-grooved or W-shaped bodies, apple-shaped profiles and topology-optimised cross-sections to strengthen aerodynamic forcing, suppress unfavourable vortex reattachment or improve low-speed response [22], [30], [34], [35], [36], [37], [38]. Other studies have used upstream or downstream flow-control components, including interference cylinders, double upstream plates, splitter plates, downstream plates, fins and auxiliary attachments, to reshape wake development and broaden the operating range [22], [39], [40]. In addition, magnetic coupling, bistability, multi-degree-of-freedom structures and hybrid piezoelectric–electromagnetic or piezoelectric–triboelectric mechanisms have been explored to reduce the effective activation threshold or enhance output over a wider wind-speed range [41], [42], [43].

These studies demonstrate that bluff-body shaping and wake control are effective routes for improving flow-induced piezoelectric energy harvesting. However, they also reveal three unresolved issues that are particularly important for weak-wind applications. First, many galloping-based harvesters still require wind speeds of approximately 2–5 m/s, or even higher, before a clear high-amplitude response is obtained. Second, some low-speed improvements are achieved by adding external upstream or downstream components, which can increase alignment sensitivity, structural complexity, and installation requirements. Third, reported performance is often compared mainly through peak voltage or peak power, while the cut-in criterion, load resistance, device dimensions, normalised output, and low-speed signal evidence are not always reported consistently. Therefore, it remains difficult to judge whether a new design improves only the peak output at moderate wind speeds or genuinely improves weak-wind accessibility.

To contextualise these issues, **Table 1** provides a study-level comparison of representative low-speed and geometry-modified piezoelectric wind energy harvesters. Each row refers to an individual published design so that the reported cut-in or onset criterion, electrical output, load condition, device dimensions and normalised performance can be traced to a specific source. Where current, power density, device size or durability information is unavailable or not directly comparable, it is explicitly identified as N/A. Because the studies use different onset definitions, electrical loads, piezoelectric materials, geometric scales and normalisation methods, the table is intended for contextual benchmarking rather than direct quantitative ranking.

Against this background, the present study proposes a reverse-C-with-tail bluff body for low-speed wind energy harvesting. The novelty of the design is not the mere addition of a tail, nor the use of a curved body alone. Rather, it lies in integrating a reverse-C cavity with a tail-guided wake-modification element. The central hypothesis is that the curved front section and rear tail jointly modify flow separation and downstream wake development in a manner that may promote stronger transverse aerodynamic asymmetry and shift the harvester toward a lower voltage-response-based cut-in wind speed. Under this interpretation, the tail should be understood as a wake-guiding component of the bluff body rather than as a separate downstream plate or external flow-control accessory.

Table 1. Study-level comparison of representative low-speed and geometry-modified piezoelectric wind energy harvesters.

Representative design	Cut-in/onset criterion	Electrical performance and load	Size/normalised output	Reporting gaps and relation to present work	Ref.
Funnel-shaped bluff body	Experimental galloping onset: 7.0 m/s	Absolute voltage, current and load: N/A in the reported comparison	Maximum reported power density: 2.34 mW cm^{-3}	Current and durability: N/A. High normalised output, but a substantially higher galloping onset than the present electrical cut-in	[30]
Curved-plate bluff body	Exact cut-in value/criterion: N/A; reported to be lower than conventional square, triangular and D-shaped sections	35.6 μW at R_L=820 kΩ; arc length = 45 mm	Complete device volume and power density: N/A	Current and durability: N/A. Closest curved-body reference, but without an integrated tail-guided wake-modification element	[35]
Square prism with double upstream flat plates	Reported cut-in reduced from 3.5 to 1.0 m/s	12 V at 1.5 m/s; power and load resistance: N/A	Downstream bluff body: 20 mm windward dimension and 85 mm height; normalised output: N/A	Current and durability: N/A. Achieves a comparable low-speed threshold but requires separate upstream components and spacing control	[39]
W-shaped bluff body	First non-zero reported voltage response at 1.5 m/s; formal criterion not explicitly standardised	7.2 V at 2 m/s; 15.2 V and 0.28 mW at 5 m/s under 820 kΩ	Bluff body: 30 ×30 mm² cross-section and 70 mm height; power density: 0.031 mW cm^{-3}	Current and durability: N/A. Integrated profile optimisation with a higher reported electrical-response threshold than the present work	[36]
Apple-shaped bluff body	Exact cut-in criterion: N/A; low-speed performance evaluated over 1.5–3.6 m/s	Maximum voltage increased by 85% relative to the square-prism reference; absolute power and load: N/A	α=120° , L=35 mm; power density: N/A	Current and durability: N/A. Demonstrates topology-based profile optimisation, but available data do not support a complete absolute ranking	[37]

Representative design	Cut-in/onset criterion	Electrical performance and load	Size/normalised output	Reporting gaps and relation to present work	Ref.
Comb-like-beam harvester	Reported cut-in reduced from 2.24 to 1.96 m/s	Power increased by approximately 171.2% relative to the conventional-beam reference at 3 m/s near the optimal resistance; absolute power/load: N/A	Complete device size and power density: N/A	Current and durability: N/A. Low-speed improvement is obtained through a more complex multi-degree-of-freedom beam rather than bluff-body wake guidance	[44]
Piezoelectric–electromagnetic hybrid galloping harvester	Piezoelectric start-up wind speed: approximately 4.8 m/s	Maximum reported piezoelectric voltage: 59.58 V under optimally matched loads	Normalised output and directly comparable total device size: N/A	Durability: N/A. Higher system complexity because magnets, coils and two transduction mechanisms are required	[43]
Reverse-C-with-tail harvester, present work	Voltage-response-based electrical cut-in: approximately 1 m/s; not the onset of fully developed galloping	V_{RMS}=46.4 V and fixed-load power = 2.152 mW at 7 m/s under R_L=1 MΩ	S5: 40 mm inner diameter, 40 mm tail length and 150 mm width; power density: N/A	Current was not independently measured; long-term durability: N/A. Integrated reverse-C cavity and tail-guided wake modification without separate upstream components	

Note: N/A indicates that the corresponding quantity was not reported in the cited study or could not be compared consistently from the available published information. The definitions of cut-in or onset wind speed differ among the studies and may be based on the first measurable voltage response, displacement growth, a model-derived critical velocity, or the establishment of galloping. Likewise, the reported power may represent a fixed-load value, a load-optimised maximum, a relative improvement over a baseline, or a normalised power density. Device size refers only to the geometric dimensions explicitly reported in the cited study and does not necessarily represent the total packaged harvester volume. Durability denotes explicit long-duration cyclic or environmental testing; N/A does not imply poor durability, but only that such evidence was not reported. Accordingly, this table is intended for contextual study-level benchmarking rather than direct quantitative ranking. For the present work, 2.152 mW is a fixed-load power output under RL=1 MΩ, not an independently optimised maximum power point.

Based on this motivation, the objectives of this work are threefold. First, preliminary CFD simulations are conducted to compare representative bluff-body geometries and to provide qualitative aerodynamic insight into how the reverse-C-with-tail configuration modifies wake development and pressure distribution. Second, wind tunnel experiments are performed using a hierarchical prototype strategy: the T-series evaluates whether tail addition is a decisive feature, the S-series examines the effect of tail length on low-speed response and electrical output, and the R-series provides a secondary comparison of curved-section thickness. Third, a reduced-order electromechanical model is introduced as an interpretive framework to reproduce the main voltage trends and relate the observed response to geometry-dependent aerodynamic coefficients. Through this combined framework, the study aims to determine whether a bluff-body harvester can achieve a repeatable voltage-response-based cut-in at approximately 1 m/s, followed by a galloping-dominated response and useful fixed-load power output over the subsequent wind-speed range.

The main contribution of this paper is therefore an experimentally validated ultra-low-cut-in design strategy for galloping-based piezoelectric energy harvesting. Compared with previous designs that mainly optimise the bluff-body cross-section, introduce external wake-control components, or rely on nonlinear/hybrid mechanisms, the present reverse-C-with-tail configuration provides an integrated geometric route for tail-guided wake modification under weak-wind conditions. The contribution is supported not only by the low cut-in wind speed itself, but also by the T/S/R experimental sequence, which clarifies the respective roles of tail addition, tail length, and curved-section refinement. The remainder of the paper is organised as follows. Section 2 presents the harvester configuration and methodology. Section 3 provides preliminary aerodynamic analysis of the proposed geometry. Section 4 reports the experimental results and discusses the effects of key geometric parameters. Section 5 introduces the reduced-order model and compares the resulting modelled voltage trends with the measured response. Finally, Sections 6 and 7 summarise the main findings, limitations and implications of the study.

2. Harvester Design and Methodology

2.1 Harvester concept and geometric rationale

To investigate whether a geometry-guided bluff-body design can achieve ultra-low voltage-response-based cut-in under weak wind conditions, a reverse-C-with-tail piezoelectric harvester was developed in this study. The design was motivated by the need to improve not only the output level after a galloping-dominated response has developed, but also the accessibility of the harvester to low-speed flow environments where many conventional galloping-based devices remain inactive. Therefore, the proposed configuration was designed with low-speed voltage-response-based cut-in as the primary target, rather than treating geometric modification as an end in itself.

The bluff body consists of two main geometric components. The front part is a reverse-C-shaped curved section characterised by its inner diameter, while the rear part is a tail extension of length L. This combined geometry is mounted at the free end of a cantilever beam, and the vibration-induced strain in the cantilever is converted into electrical output through an attached piezoelectric patch. As in most cantilever-based piezoelectric energy harvesters, the first bending mode is expected to dominate the response; therefore, the piezoelectric layer is positioned near the clamped end to maximise strain utilisation and voltage generation. In all experiments, the incoming wind is directed horizontally from left to right, as illustrated in **Fig. 1(a)**.

The design rationale is that the curved front section controls the primary flow separation behaviour, while the rear tail modifies the wake development behind the body. Compared with a tailless configuration, the tailed geometry is expected to create a more favourable aerodynamic condition for earlier transverse instability. In this sense, the tail is introduced not simply as an added geometric feature, but as the main design element intended to shift the harvester towards a lower voltage-response-based cut-in regime. The subsequent experimental comparisons were therefore organised to distinguish the effect of tail addition from the further effects of tail length and curved-section thickness.

The following subsections describe the fabrication and measurement procedure, define the voltage-response-based cut-in criterion, and then introduce the T-, S- and R-series prototypes used to separate the effects of tail addition, tail length and curved-section thickness.

2.2 Prototype fabrication and material selection

All prototypes were designed in SolidWorks and fabricated by 3D printing using a Prusa MK3S printer. Additive manufacturing was adopted because it allows rapid preparation of multiple geometric variants with good repeatability and avoids assembly-related inconsistencies in the bluff-body shape. This was particularly useful in the present study, where several closely related configurations had to be compared under the same test conditions.

The prototypes were printed using polylactic acid (PLA), which has a Young's modulus of approximately 2.7 GPa. Although some previous studies have employed lightweight metallic materials, PLA was considered sufficient here because the purpose of the work was to compare the relative aerodynamic and electromechanical behaviour of different geometries rather than to assess long-term structural durability. The use of 3D printing also enabled the bluff body to be manufactured as an integrated component, which helped maintain geometric consistency among the tested models.

A commercial piezoelectric patch (Smart Material M-2807-P2) was bonded near the clamped end of the cantilever beam. The voltage generated by the patch was measured using a digital oscilloscope (TBS1072B), with the electrodes connected through two probes. A previous study on a related curved-plate piezoelectric wind energy harvester reported an optimal external load resistance of approximately 820 kΩ, with only limited variation over the investigated wind-speed range [35]. Informed by this result, a fixed external resistance of R_L=1 MΩ was adopted in the present study to provide a common electrical condition for direct comparison among the prototype configurations. This resistance was not independently optimised for the individual prototypes. Accordingly, all reported power values are fixed-load outputs under R_L=1 MΩ, rather than independently optimised maximum power points.

The aerodynamic force acting on the harvester was measured using an ATI Nano43 six-axis force/torque sensor mounted on an adjustable base in the wind tunnel. This allowed the force response to be analysed together with the electrical output, which is important for interpreting whether improvements in voltage generation are associated with stronger aerodynamic excitation. A schematic diagram of the experimental setup is shown in **Fig. 1(b)**. The experiments were carried out in a wind tunnel with an operating section of 1.2 × 1.2 × 3 m^3, and the main wind tunnel specifications are summarised in Supplementary **Table S1**.

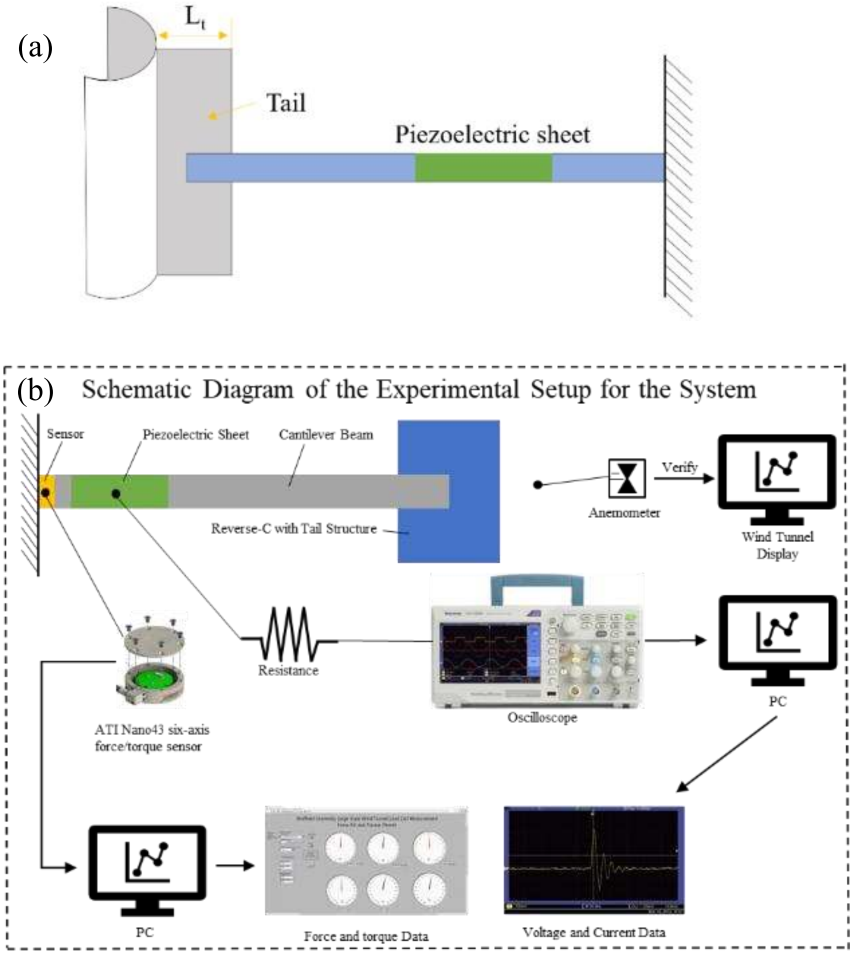

Figure 1. (a) Schematic of the proposed reverse-C-with-tail piezoelectric harvester; (b) Schematic of the experimental setup, including the wind tunnel arrangement, cantilever-based harvester, force measurement system, and voltage acquisition circuit.

The S-series models were tested over the wind-speed range of 1–7 m/s because they were intended to examine low-speed response and cut-in behaviour. By contrast, the T-series and R-series were mainly tested over 3–7 m/s, where their aerodynamic differences were more stable and easier to compare. The upper limit of 7 m/s was adopted because it remains relevant to weak-flow harvesting applications while avoiding excessive output voltage that may reduce measurement accuracy. These settings ensured that the experiments focused on a practically meaningful and comparable operating range.

2.3 Cut-in wind speed definition and experimental data processing

Because the main focus of this work is low-speed accessibility, the cut-in condition was defined from the electrical response of the harvester. In this manuscript, cut-in wind speed refers to the electrical cut-in wind speed determined from the measured voltage response. It is defined as the lowest tested wind speed at which a measurable RMS voltage response was consistently observed in repeated measurements. A response was regarded as measurable when the voltage fluctuation was clearly distinguishable from the low-amplitude noise-dominated baseline response and appeared consistently in repeated tests. Since the wind speed was varied in discrete increments, the reported value of approximately 1 m/s should be interpreted as the lowest tested wind speed satisfying this voltage-response criterion, rather than as an exact continuous threshold.

For the experimental data reported in the following sections, each wind-speed condition was tested at least three times. The RMS voltage was obtained from the stable portion of the recorded voltage signal after the initial transient response was excluded. The mean value was used for comparison, and the experimental scatter was quantified using the standard deviation. The fixed-load power output was calculated from the corresponding RMS voltage under the external resistance used in the experiment. The dominant vibration frequency was mainly extracted from the force signal when the force response was sufficiently stable for reliable frequency identification. At very low wind speeds, where the force signal was too weak or noise-dominated, the frequency was not reported unless a stable oscillatory component could be identified reliably.

This definition of cut-in wind speed is different from the onset of a fully developed galloping response determined from force-frequency data. At very low wind speeds, especially 1–2 m/s, the force response of some configurations was too weak for reliable frequency extraction. The voltage signal, however, still provides useful low-speed response information. In the tailless and short-tail cases, especially S0–S2, the low-speed voltage histories remained weak and noise-dominated, so a stable oscillation frequency could not be identified reliably. In contrast, the longer-tail configurations, particularly S3–S5, exhibited clearer periodic voltage fluctuations at low wind speeds, indicating that the electrical response became progressively more organised as the tail length increased. Therefore, the low-speed cut-in assessment was based primarily on the repeatable RMS voltage response and supporting voltage time histories.

2.4 Parametric prototype configurations

To distinguish the roles of different geometric parameters, the prototypes were divided into three groups: the T-series, the S-series and the R-series. The T-series isolates the effect of tail addition, the S-series examines progressive tail extension, and the R-series provides a secondary comparison of curved-section thickness under similar tail-length ratios.

The T-series was designed to isolate the influence of adding a tail to the curved bluff body (see **Fig. 2 (a1)**). The T1 model has the same principal dimensions as the curved-plate design reported by Zhou et al. [35], whereas the T2 model introduces a rear tail of 22.75 mm. This tail length was selected with reference to the ratio reported by Song et al. [22], where a cylinder-diameter-to-splitter-plate-length ratio of 0.65 was found to be favourable. Although the present body is semi-circular rather than cylindrical, the same ratio was used here as a physically informed reference. The purpose of this series was therefore to determine whether the tail itself acts as a decisive aerodynamic component rather than as a minor structural modification.

The S-series was the primary parametric group used to evaluate the role of tail length in low-speed energy harvesting performance (**Fig. 2(a3)**). This series contains six models, denoted S0–S5, all with the same inner diameter of 40 mm and the same width of 150 mm, but with tail lengths of 0, 10, 20, 26, 30, and 40 mm, respectively. These dimensions correspond to tail-length-to-inner-diameter ratios of 0, 0.25, 0.5, 0.65, 0.75, and 1.0. Because all S-series models share the same basic reverse-C concept and differ primarily in tail extension, this group provides the clearest basis for evaluating whether the main advantage of the proposed design lies in reducing cut-in wind speed rather than only enhancing output at higher velocities.

The R-series was introduced to assess the influence of curved-section thickness on harvester performance (**Fig. 2(a2)**). This series was originally intended to include several models with the same tail-length ratios as the corresponding S-series cases but with a thinner curved section. In practice, however, only two models, R1 and R2, were successfully fabricated. The remaining intended prototypes either failed during printing or were too fragile to preserve structural integrity, because the curved thickness was only 0.5 mm. The two successful R-series models were later compared with S4 and S5 to evaluate how thickness variation affects the aerodynamic and electrical response. The R-series therefore serves as a secondary optimisation comparison rather than the main experimental set.

2.5 Geometric dimensions and structural considerations

The detailed geometric parameters of all prototypes are listed in **Table 2**, including curve thickness, curve inner diameter, tail length, and frontal width. In the T-series, both models have a curved thickness of 0.5 mm and an inner diameter of 35 mm, with tail lengths of 0 and 22.75 mm and a width of 100 mm. In the R-series, both models have a curved thickness of 0.5 mm and an inner diameter of 40 mm, with tail lengths of 30 and 40 mm and a width of 150 mm. In the S-series, all models have a curved-section thickness of 2 mm and an inner diameter of 40 mm, while the tail length varies from 0 to 40 mm and the width remains 150 mm. To clarify the structural changes introduced by tail extension, the mass of each printed S-series bluff body was measured repeatedly using a digital balance with a resolution of 0.1 g. The streamwise centre-of-gravity coordinate was obtained separately from the SolidWorks mass-properties calculation based on the final CAD geometry. The measured masses and CAD-derived centre-of-gravity coordinates are reported in **Table 2**.

The frontal width determines the projected area directly exposed to the incoming airflow and therefore influences the overall aerodynamic loading. A larger width can potentially increase the available aerodynamic force and the resulting energy harvesting capability, although it may also increase drag. In addition, a rear mounting hole was incorporated into the design to connect the bluff body to the cantilever beam, and the tail-end thickness was fixed at 4 mm in the attachment region to ensure sufficient local stability. These structural details were necessary to ensure that the tested geometric variations could be compared without compromising mounting reliability during the experiments.

It should also be noted that geometric modification inevitably interacts with the dynamic response of the harvester. Increasing the tail length is expected to modify the separated wake and strengthen the transverse excitation, but it also changes the structural properties of the bluff-body–beam system. As shown in **Table 2**, the measured bluff-body mass increases from 22.5 g for S0 to 47.2 g for S5, while the CAD-derived centre-of-gravity x-coordinate shifts from 18.284 mm to 30.336 mm. These changes indicate that tail extension increases the physical mass of the printed bluff body and shifts its nominal mass distribution downstream. Both effects can modify the inertial contribution of the bluff body and influence the coupled vibration characteristics of the bluff-body–beam system. The mass trend is supported by repeated physical measurements, whereas the centre-of-gravity trend should be interpreted as a CAD-derived structural estimate rather than as an uncertainty-resolved physical measurement. Therefore, the S-series should be interpreted as a controlled tail-length study under consistent reverse-C geometry, material, frontal width, inner diameter and mounting scheme, rather than as a complete separation of aerodynamic and structural effects. The parameter ranges adopted here were selected to balance aerodynamic effectiveness, fabrication feasibility, structural robustness and experimental repeatability, thereby providing a reliable basis for the results discussed in the following sections.

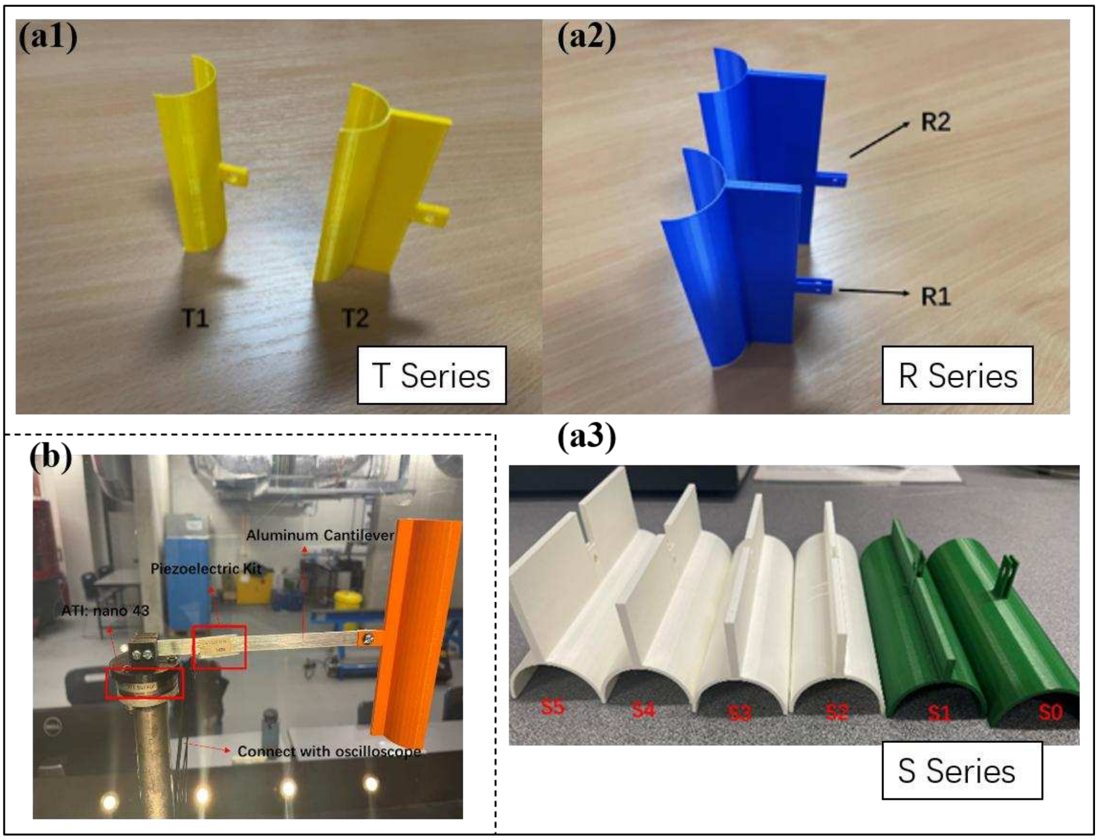

Figure 2. Geometric design and prototype series of the proposed harvester: **(a1)** T-series for evaluating the effect of tail addition; **(a2)** R-series for examining the effect of curved-section thickness; **(a3)** S-series for investigating the effect of tail length; **(b)** Representative fabricated prototypes and mounting configuration.

Table 2. Geometric parameters of the T-, R-, and S-series prototypes and measured mass/CAD-derived centre-of-gravity parameters of the S-series models.

Model code	Curve thickness (mm)	Curve inner diameter (mm)	Tail length (mm)	Width (mm)	Measured mass (g)	CAD-derived CG x-coordinate (mm)	CAD-derived CG shift from S0 (mm)
T1	0.5	35	0	100	N/A	N/A	N/A
T2	0.5	35	22.75	100	N/A	N/A	N/A
R1	0.5	40	30.00	150	N/A	N/A	N/A
R2	0.5	40	40.00	150	N/A	N/A	N/A
S0	2	40	0	150	22.5	18.284	0
S1	2	40	10.00	150	28.7	20.573	2.289
S2	2	40	20.00	150	34.9	22.005	3.721
S3	2	40	26.00	150	38.6	24.145	5.861
S4	2	40	30.00	150	41.0	27.213	8.929
S5	2	40	40.00	150	47.2	30.336	12.052

Note: Masses were measured repeatedly using a digital balance with a resolution of 0.1 g, and no repeatability variation was resolved at this resolution. The CG coordinates were obtained from the SolidWorks mass-properties calculation and are referenced to a common CAD origin along the streamwise x-axis. Possible deviations caused by printing tolerances and material-distribution variations are discussed in Section 2.5.

3. Preliminary CFD Analysis and Aerodynamic Interpretation

3.1 Purpose and scope of the preliminary CFD analysis

To clarify the aerodynamic rationale of the proposed reverse-C-with-tail configuration, preliminary computational fluid dynamics (CFD) simulations were carried out before detailed experimental interpretation. The purpose of this numerical analysis was not to provide a high-fidelity quantitative prediction of the fully coupled fluid-structure response, but rather to serve as a qualitative diagnostic tool for identifying the main flow features associated with the proposed geometry. In particular, the CFD analysis was intended to examine whether the addition of a tail can create a more favourable aerodynamic environment for low-speed response development by modifying wake evolution, pressure distribution, and the local recirculation pattern.

The present study focuses on the question of whether a geometry-guided bluff-body design can intentionally reduce the cut-in wind speed of a galloping-based piezoelectric harvester. For this purpose, it is sufficient at this stage to establish a physically plausible aerodynamic explanation for the improved low-speed response observed later in the experiments. The CFD analysis is therefore organised in two steps. First, representative bluff-body geometries are compared under the same inflow condition to examine whether the reverse-C-with-tail configuration produces a stronger transverse lift response than conventional reference shapes. Second, selected S-series cases are analysed to identify how tail addition and tail extension modify the local wake, pressure field and lift-coefficient response. The resulting observations are then interpreted together with the wind tunnel measurements in Section 4.

3.2 Numerical model and computational setup

The preliminary numerical simulations were conducted in ANSYS Fluent using a two-dimensional unsteady Reynolds-averaged Navier–Stokes formulation. The same fixed-body numerical framework was used for both the representative geometry comparison and the S-series tail-length analysis. In all cases, the bluff body was treated as a fixed body and a static mesh was used; therefore, the simulations were intended to provide semi-quantitative aerodynamic diagnostics rather than a fully coupled fluid–structure prediction. The standard k-ε turbulence model was adopted as a practical compromise between computational cost and wake-resolution capability for the present two-dimensional parametric comparison. The turbulence intensity and turbulent viscosity ratio at the inlet were set to 5% and 10, respectively.

For the S-series simulations used to interpret the effect of tail length, the computational domain was a rectangular region of 200 cm × 100 cm. This domain size was selected to reduce the influence of confinement and to ensure that the dominant wake structures could be captured without strong wall interference. The overall domain arrangement is shown in Supplementary **Fig. S1**. The centre of the curved body was located on the horizontal centreline of the domain and positioned 50 cm downstream of the inlet. Air was modelled with a density of 1.225 kg/m^3 and a dynamic viscosity of 1.79×10^{-5} kg/(m·s). The left boundary was set as a velocity inlet, the right boundary as a pressure outlet, and the upper and lower boundaries as fixed walls. The inflow velocity was varied from 3–7 m/s for the S-series comparison, and the time step was set to 0.001 s.

Triangular elements were used for the fluid domain, with local refinement around the bluff body and the tail region. The mesh quality was checked using element quality, aspect ratio, Jacobian ratio, skewness and orthogonal quality. For the S0 reference model, the average element quality was 0.964, the average aspect ratio was 1.197, the Jacobian ratio was 1.000, the skewness was 0.054 and the orthogonal quality was 0.966. A mesh-independence check was also performed by comparing five mesh densities, from 5874 to 87865 elements. The peak lift coefficient changed by more than 40% when the mesh was refined from the coarse cases to the medium mesh, but the variation became less than 5% after the mesh reached approximately 22652 elements. Therefore, the medium mesh was selected for the subsequent S-series simulations to balance numerical accuracy and computational cost. The details of CFD setup are shown in Supplementary **Table S2**.

In the representative geometry comparison, several bluff-body shapes were examined, including a circular section associated with vortex-induced vibration, a square section often used as a reference geometry for galloping studies, a curved-plate configuration and the proposed reverse-C-with-tail design.

All candidate geometries in the preliminary comparison were simulated under the same inflow velocity of 4 m/s. This condition was chosen as an intermediate reference velocity at which the relative aerodynamic response of the different shapes could be compared clearly. The lift coefficient histories were then extracted and compared in order to assess the ability of each geometry to generate transverse aerodynamic instability. A geometry that exhibits stronger and more rapidly developing lift fluctuations is considered to possess greater potential for promoting low-speed aeroelastic response development in the physical harvester.

3.3 Qualitative comparison with representative bluff-body geometries

The first stage of the CFD analysis aimed to determine whether the proposed reverse-C-with-tail geometry exhibits a distinct aerodynamic advantage relative to representative bluff-body shapes. **Fig. S2(a)** compares the stabilised lift-coefficient responses of the circular, square, and curved-plate configurations at 4 m/s. Among these reference cases, the curved plate shows a more pronounced lift response than the circular and square bodies, indicating that this family of geometry already provides a more favourable aerodynamic basis for transverse vibration. This observation is consistent with the motivation for building the present design on a curved-body concept rather than on a conventional square or circular section.

A further comparison between the curved-plate configuration and the proposed reverse-C-with-tail design is shown in Supplementary **Fig. S2(b)**. Under the same inflow condition, the reverse-C-with-tail geometry develops a stronger lift response and reaches a pronounced fluctuation state more rapidly than the curved plate. In qualitative terms, this suggests that the proposed geometry is more effective at producing the aerodynamic asymmetry required for galloping-type behaviour. Since the two bodies share the same general curved-body concept, the stronger lift-coefficient fluctuation of the reverse-C-with-tail case is consistent with an aerodynamic influence of the tail on downstream wake development. However, the present fixed-body comparison does not independently quantify the individual wake mechanisms responsible for this difference.

This comparison does not by itself prove that the proposed harvester will achieve a lower voltage-response-based cut-in wind speed in the experiment, because the simulations are performed for fixed bodies in a simplified two-dimensional setting. However, it does provide an important first indication that the reverse-C-with-tail concept is aerodynamically meaningful rather than an arbitrary geometric modification. The stronger lift fluctuation observed numerically justifies further examination of the local flow structures responsible for this behaviour.

3.4 Flow-field comparison between tailless and tailed configurations

To examine the specific aerodynamic role of the tail, the analysis was then focused on representative models derived from the experimental S-series. Among these models, S0 and S1 were selected for detailed comparison because they share the same basic geometry except for the presence of a short tail extension. This pair therefore provides a clear basis for isolating how tail addition modifies the flow pattern around the bluff body. The objective of this comparison is not to establish an exact quantitative relationship between CFD force levels and measured aerodynamic loads, but to identify the flow mechanisms that can plausibly explain the experimentally observed reduction in cut-in wind speed.

The vector and pressure contours of the S0 model are presented in **Fig. 3(a)**. For the tailless case, the incoming flow separates near the leading edge and generates alternating inner circulations above and below the body. These vortical structures produce fluctuating pressure distributions on the upper and lower surfaces, indicating the presence of an unstable aerodynamic environment that can potentially trigger transverse vibration. In the selected S0 contour snapshots, the low-pressure zone and the internal recirculating pattern appear relatively compact. This contour-level observation qualitatively suggests a comparatively weak upper–lower pressure contrast, but neither the pressure difference nor the recirculation length was extracted as a scalar quantity.

In contrast, the selected S1 contours in **Fig. 3(b)** qualitatively suggest a more extended recirculating-flow pattern and a more pronounced upper–lower pressure contrast around the body. The flow beneath the bluff body appears to interact with the tail and to redirect the downstream flow pattern, with a more extensive low-pressure zone visible near the lower side in the plotted snapshot. These visual observations are qualitatively consistent with stronger transverse aerodynamic forcing, which is assessed more directly through the lift-coefficient histories rather than through a scalar pressure-difference or recirculation-length metric. From the viewpoint of low-speed response development, this is important because low-speed activation requires the structure to experience a sufficiently strong and persistent aerodynamic asymmetry even before large-amplitude oscillation has fully developed. The CFD results therefore support the idea that the tail improves not only the magnitude of the aerodynamic response, but also the aerodynamic accessibility of the harvester to weaker flow conditions.

Another notable difference between the two configurations is that the added tail appears to regulate the wake in a more organised manner. In the tailless case, the separated flow remains relatively compact and the fluctuating region is concentrated close to the curved body. With the tail present, the selected contour and streamline snapshots show a recirculating pattern that appears to extend further downstream, together with a more visible contrast between the upper- and lower-side pressure fields. These qualitative observations are consistent with the tail acting as a wake-shaping element rather than merely increasing the projected area of the bluff body. However, the present analysis does not quantify the recirculation length or pressure difference. Such a role is consistent with the central design idea of the present work, namely that tail addition should be understood as the primary aerodynamic mechanism behind the reduction in cut-in wind speed.

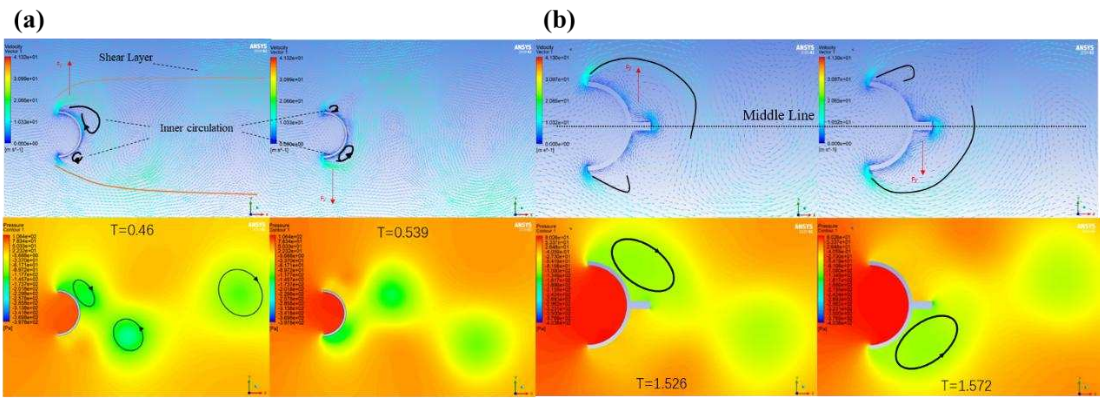

Figure 3. Vector and pressure contours of the S0 and S1 models at representative phases of the lift-coefficient cycle: (a) S0 at the C_L peak (t=0.460 s) and trough (t=0.539 s); (b) S1 at the C_L peak

(t=1.526 s) and trough (t=1.572 s).

3.5 Streamline-based interpretation of tail-induced instability

To further visualise the aerodynamic behaviour of the tailed configuration, the velocity streamlines of the S1 model are presented in Supplementary **Fig. S3**. These results provide a qualitative snapshot of vortex formation and downstream flow evolution around the reverse-C-with-tail geometry; they are not used to determine an independent vortex-shedding frequency. When a circulation region develops beneath the body, the local flow accelerates and generates a pronounced low-pressure zone. At the same time, the detached vortex affects the upper-surface flow and promotes upward deflection rather than immediate reattachment to the bluff body. This alternating streamline pattern is qualitatively consistent with a time-varying upper–lower pressure contrast and an aerodynamic moment favourable to transverse oscillation. Because the pressure difference was not extracted as a scalar metric, the interpretation remains contour-based.

This mechanism is directly relevant to the weak-flow response targeted in the present study. A useful low-speed electrical response requires the bluff body to develop persistent transverse aerodynamic asymmetry before a large-amplitude galloping-dominated response is fully established. The S1 streamline pattern qualitatively suggests that the tail redirects the downstream flow, produces a more extended recirculating pattern and may reduce immediate shear-layer reattachment in the selected snapshot. These features are interpreted as possible contributors to the observed transverse response, rather than as independently quantified aerodynamic metrics. These observations provide qualitative mechanistic support for the low-cut-in design strategy proposed in this study.

The CFD evidence is interpreted at two distinct levels. The lift-coefficient histories, peak lift coefficients, response times and dominant frequencies of the lift-coefficient oscillations are treated as extracted quantitative outputs. By contrast, the vector, pressure and streamline fields are used only for qualitative flow-pattern interpretation. Pressure difference, recirculation length and vortex-shedding frequency were not extracted as independent scalar metrics. Accordingly, statements concerning pressure contrast, recirculating-flow extent, reattachment and vortex development are framed as qualitative observations, whereas the lift-coefficient and response-time trends provide the main quantitative support.

Because the model is two-dimensional and fixed, the simulations do not include spanwise effects, end effects or motion-induced feedback between the cantilever and the surrounding flow. Nevertheless, they are sufficient to identify the relative aerodynamic consequences of tail addition and to provide a physical bridge between the harvester design introduced in Section 2 and the experimental response presented in Section 4.

3.6 Aerodynamic implications for low-speed response development

Taken together, the preliminary CFD results suggest that the tail affects the proposed harvester primarily by reshaping the wake rather than simply increasing the projected area.

The pressure contours and streamline fields qualitatively suggest that tail addition produces a more extended recirculating-flow pattern and a more pronounced upper–lower pressure contrast around the bluff body. These visual observations are not treated as scalar measurements. The lift-coefficient histories provide separate quantitative evidence that the tailed configurations generate stronger transverse aerodynamic fluctuations. In the S-series simulations, the peak lift coefficient increased with tail length; at 7 m/s, the peak C_L of S5 was approximately 57% higher than that of the tailless S0 model. The response-time comparison also showed that longer-tail configurations developed noticeable lift fluctuations earlier, with the S5 curve beginning to fluctuate at around 0.02 s, compared with approximately 0.10 s for S0.

At the same time, the CFD results suggest a trade-off between stronger transverse aerodynamic forcing and a lower characteristic response frequency. The dominant frequency of the lift-coefficient oscillation decreased as the tail length increased. This trend coincides with the qualitatively more extended recirculating-flow patterns visible in the longer-tail cases and may reflect a change in the characteristic wake-development timescale. However, neither recirculation length nor vortex-shedding frequency was independently extracted, so this explanation should be regarded as qualitative. Therefore, the numerical results should not be interpreted as showing that longer tails are always superior in every respect. Instead, they indicate that tail extension can strengthen the aerodynamic forcing associated with low-speed response development while also modifying the wake timescale.

Overall, the CFD analysis supports the central hypothesis of the present work: adding a tail to the reverse-C bluff body creates a more favourable aerodynamic environment for low-speed voltage-response-based cut-in and subsequent galloping-dominated response development. This does not replace the need for experimental validation, because the CFD model is fixed-body and two-dimensional. However, it provides a coherent flow-based explanation for why the proposed design is expected to outperform the corresponding tailless configuration in the low-speed regime. The next section therefore turns to wind tunnel experiments to examine whether this aerodynamic advantage is reflected in measurable improvements in cut-in wind speed, lift response, voltage output and fixed-load power generation.

4. Experimental Results and Discussion

4.1 Experimental scope and evaluation logic

The experiments were organised to evaluate whether the proposed reverse-C-with-tail concept can shift a galloping-based piezoelectric harvester into an ultra-low-cut-in operating regime while maintaining useful electrical output over the subsequent wind-speed range. Rather than treating the T-series, S-series and R-series as separate comparisons, they were designed to form a hierarchical evaluation sequence. The T-series first examines whether adding a tail fundamentally changes the harvester response relative to a comparable tailless curved-body baseline. The S-series then investigates how progressive tail extension affects cut-in wind speed, lift response, vibration frequency, voltage generation and fixed-load power output. Finally, the R-series provides a secondary comparison of curved-section thickness after the main tail-enabled mechanism has already been established.

This sequence is important for clarifying the logic of the experimental design. The central contribution of the present study is not simply that a modified bluff body produces larger output after galloping has already developed. Instead, the key question is whether the proposed geometry can make the harvester electrically active under weaker wind conditions while still producing useful output at higher wind speeds. Accordingly, the following discussion first isolates the effect of tail addition, then examines tail-length dependence in the low-speed regime, and finally considers whether curved-section thickness can further refine the reverse-C-with-tail design. The S-series results are therefore discussed over 1–7 m/s to capture the low-speed cut-in behaviour and subsequent output growth, whereas the T-series and R-series comparisons are mainly discussed over 3–7 m/s, where the comparative trends are more stable and easier to resolve.

4.2 Effect of tail addition

The first issue examined experimentally is whether the tail acts as a decisive aerodynamic component rather than a minor geometric appendage. To isolate this effect, the T-series models were tested over the wind-speed range of 3–7 m/s. Supplementary **Fig. S4(a)** shows the lift-force histories of T1 and T2 at 5 m/s. Both models exhibit approximately sinusoidal fluctuations, indicating periodic transverse response under the imposed flow condition. Small irregularities are still visible in the signals, which may be associated with tunnel turbulence and minor structural instability, particularly in the lighter tailless case. However, the overall difference between the two models is clear: the tailed configuration exhibits a larger force response.

At 5 m/s, T2 produces a higher peak lift force than T1, although its vibration frequency is slightly lower. This difference is important because it shows that the tail does not simply accelerate the response; rather, it strengthens the aerodynamic excitation and shifts the system towards larger-amplitude motion. Across the full 3–7 m/s range, the same trend is maintained. As shown in Supplementary **Fig. S4(b)**, T2 consistently produces higher peak lift force than T1 at every tested wind speed. At 7 m/s, the peak lift reaches 2.29 N for T2, compared with only 1.37 N for T1. This substantial increase confirms that the tail intensifies the transverse aerodynamic loading acting on the harvester.

The electrical response follows the same pattern. Although T1 exhibits a slightly higher vibration frequency, its smaller oscillation amplitude results in much lower RMS voltage. At 7 m/s, T2 reaches an RMS voltage of 6.6 V, whereas T1 delivers only 1.47 V. This contrast indicates that frequency alone is not the dominant factor governing harvesting performance in the present system. Instead, the stronger aerodynamic instability induced by the tail generates larger beam deformation and thus higher piezoelectric output.

From the viewpoint of the present paper, the most important implication of the T-series is that the tail is not an incidental structural addition. It fundamentally alters the aerodynamic behaviour of the harvester and enables a much stronger coupled response. Although the T-series is not used to identify the exact cut-in threshold, it provides direct experimental evidence that tail addition is the key design feature promoting low-speed electrical activation and strengthening the subsequent galloping-dominated response. This conclusion establishes the basis for the more detailed tail-length study presented next.

4.3 Effect of tail length

The S-series was used to evaluate how progressive tail extension affects aerodynamic forcing, vibration frequency, low-speed voltage response and fixed-load electrical output. The discussion is organised into four parts: lift response, frequency response, representative low-speed voltage time histories, and voltage/power output.

Lift response

Fig. 4(a) shows that the peak lift force increases progressively as the tail length increases. Among all S-series models, S5 exhibits the largest force response and the strongest aerodynamic excitation, whereas the tailless S0 model displays only weak periodic oscillation. This monotonic increase indicates that extending the tail strengthens the transverse aerodynamic loading of the harvester. The trend is consistent with the two levels of CFD evidence presented in Section 3. The contour and streamline fields qualitatively suggest a more extended recirculating-flow pattern and a more pronounced pressure contrast for the longer-tail cases, while the extracted peak lift coefficients quantitatively increase with tail length.

A further comparison between the simplified CFD prediction and the wind tunnel measurements supports the same tail-length trend, although the absolute values should not be interpreted as direct one-to-one predictions. In the fixed-body simulations, the calculated lift force increased from 0.22 N for S0 to 0.37 N for S5 at 3 m/s, and from 1.34 N for S0 to 2.11 N for S5 at 7 m/s. The corresponding experimental lift forces also increased with tail length, from 0.59 N for S0 to 1.86 N for S5 at 3 m/s, and from 1.03 N for S0 to 2.40 N for S5 at 7 m/s. Therefore, both CFD and experiment show the same main tendency: longer tails generate stronger transverse aerodynamic loading.

The discrepancy between the simulated and measured force levels is expected because the two results are based on different physical conditions. The CFD model treats the bluff body as a fixed two-dimensional body, whereas the experiment captures the coupled motion of the bluff body mounted on a cantilever beam. Once the harvester begins to deflect, drag-related loading can contribute to the measured transverse response through the changing orientation and motion of the body, especially for longer-tail configurations. This motion-induced contribution is not included in the fixed-body CFD model. Therefore, the CFD results are best understood as a semi-quantitative aerodynamic explanation for the observed experimental trends, rather than as an independent high-fidelity prediction of the measured force level.

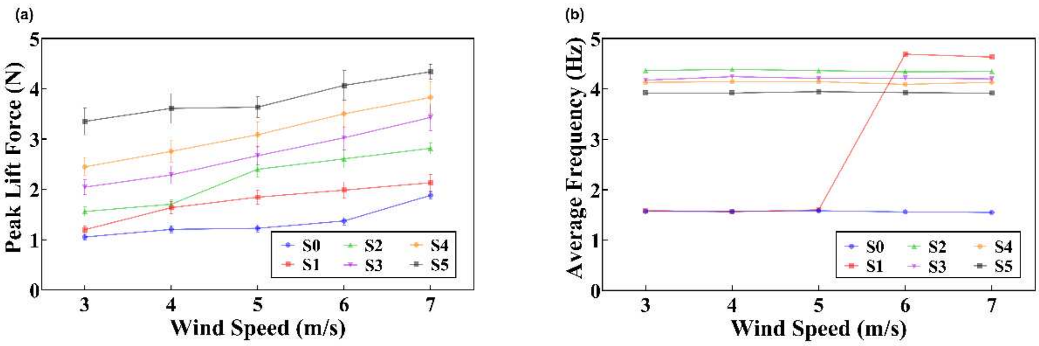

Figure 4. Effect of tail length in the S-series: **(a)** peak lift force of S0–S5 at 3–7 m/s; **(b)** average vibration frequency of S0–S5 at 3–7 m/s. Error bars represent standard deviations from repeated measurements.

Frequency response

The corresponding vibration frequencies are shown in **Fig. 4(b)**. Apart from a local irregularity for S1, the general trend is that the vibration frequency decreases as the tail length increases. The S1 frequency jump should not be interpreted as evidence of a separate response mechanism. Compared with the longer-tail configurations, S1 produces a relatively weak force response, so the extracted dominant frequency is more sensitive to signal noise, the selected measurement window and small local fluctuations in the force history. The S1 value is therefore treated as a local frequency-identification irregularity rather than as a robust physical trend.

The overall frequency reduction supports the view that the tail-length effect is not purely aerodynamic. As shown in **Table 2**, increasing the tail length from S0 to S5 increases the measured bluff-body mass from 22.5 g to 47.2 g and shifts the CAD-derived centre-of-gravity coordinate downstream by 12.052 mm. These changes are consistent with an increased inertial contribution of the bluff body and can contribute to the observed reduction in the coupled vibration frequency. However, the CAD-derived centre-of-gravity positions were not independently verified by physical balancing measurements, and the relative aerodynamic and structural contributions to the frequency change were not quantified separately. At the same time, the longer tail modifies the separated wake and may change the aerodynamic damping. Therefore, the S-series response should be interpreted as a coupled aero-structural effect: tail extension strengthens wake-induced excitation and low-speed accessibility, while the accompanying mass redistribution contributes to the reduction in vibration frequency.

This observation also highlights an important trade-off. A longer tail is beneficial for promoting stronger excitation and lowering the defined cut-in threshold, but it does not necessarily improve every dynamic indicator simultaneously. The present system therefore does not exhibit a simple "longer is always better" relationship in every respect. Instead, tail extension increases amplitude and output while gradually lowering frequency, suggesting that structural design must balance response intensity against dynamic rate.

Low-speed voltage time histories

At very low wind speeds, especially 1–2 m/s, the force response of some configurations remained too weak for reliable frequency extraction. For this reason, the corresponding force-based frequency data were not included in **Fig. 4**. However, this does not mean that all low-speed electrical responses were indistinguishable. Representative voltage time histories are shown in **Fig. 5** to support the voltage-response-based cut-in assessment.

Fig. 5(a) compares S0 and S5 at 1 m/s. The S0 signal remains at a low-amplitude, noise-dominated level and does not show a reliable periodic response, whereas the S5 signal exhibits a distinguishable oscillatory voltage fluctuation under the same wind condition. **Fig. 5(b)** further shows the voltage response of S5 at 1, 2 and 3 m/s. The oscillation amplitude increases progressively with wind speed, and the waveform becomes increasingly distinguishable from the low-speed noise background. These time-domain results support the use of approximately 1 m/s as the voltage-response-based cut-in wind speed of the longest-tail configuration under the present testing protocol.

This voltage-based cut-in criterion does not imply that a fully developed force-based galloping response is already established at 1 m/s. Rather, the 1 m/s result for S5 indicates repeatable electrical activation with a recognizable voltage oscillation. The subsequent response is described as galloping-dominated because the oscillation becomes more sustained as wind speed increases, the lift and voltage amplitudes increase systematically over a broad wind-speed range, and the response level depends strongly on bluff-body geometry, especially tail length. This behaviour is different from a purely noise-dominated perturbation or an isolated VIV-type lock-in response, and is consistent with the contour-level indication that the tail modifies the separated-flow pattern, together with the quantitative lift-coefficient trend showing stronger transverse aerodynamic fluctuations for the tailed configurations.

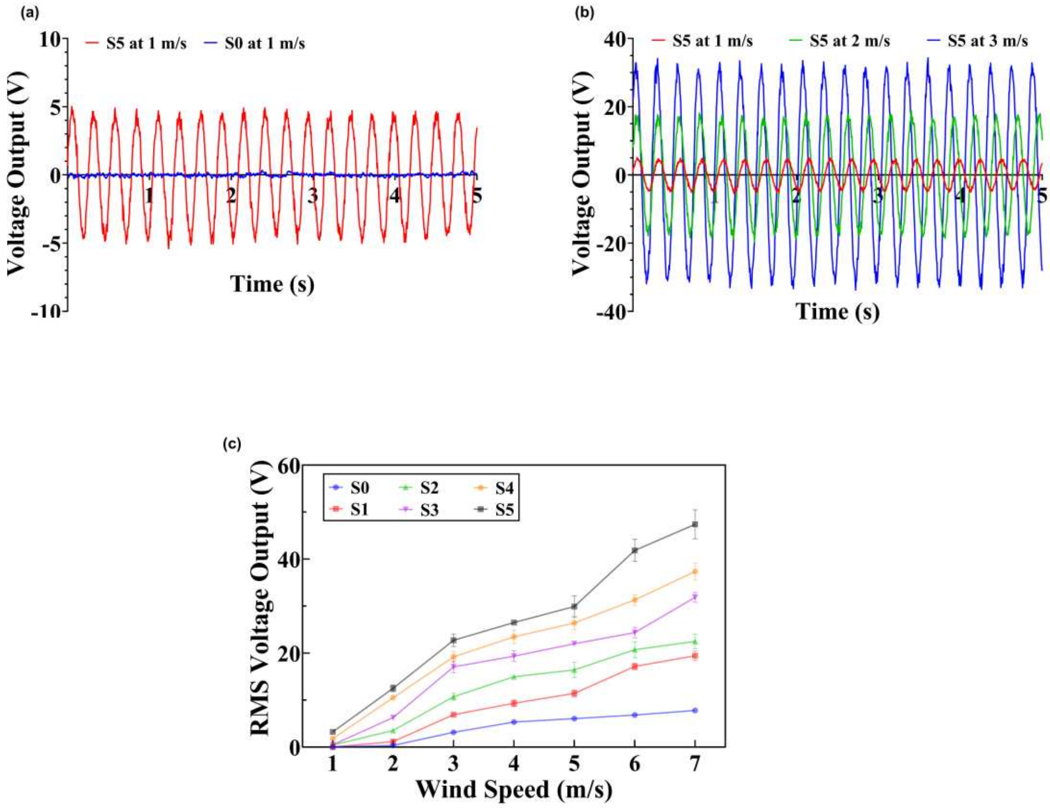

Figure 5. Representative low-speed voltage time histories: (a) comparison between S0 and S5 at 1 m/s; (b) voltage response of S5 at 1, 2 and 3 m/s. (c) RMS voltage response of the S-series models over the wind-speed range of 1–7 m/s. Error bars represent standard deviations from repeated measurements.

Voltage and fixed-load power output

The RMS voltage curves shown in **Fig. 5(c)** closely follow the lift-force trends, and the repeated-test scatter does not change the overall ranking of the S-series configurations. For all models, the voltage increases with wind speed, with a more pronounced rise beyond approximately 4 m/s. Across the tested range, the longer-tail configurations consistently outperform the shorter-tail and tailless models. In particular, S5 provides the strongest response, reaching about 46 V at 7 m/s, while S0 remains below 8 V. This large performance gap indicates that tail extension improves the coupled aeroelastic and electromechanical response of the harvester.

The low-speed behaviour is especially important. Consistent with the time-domain evidence in **Fig. 5**, the longer-tail models, especially S3–S5, exhibit measurable voltage responses at 1–2 m/s, whereas the shorter-tail and tailless configurations remain weak or noise-dominated. This confirms that tail extension improves not only the output level at moderate wind speeds, but also the accessibility of the harvester to weaker wind environments.

Table 3. Mean fixed-load power output of the S-series models at different wind speeds under R_L=1 MΩ (mW).

	1 m/s	2 m/s	3 m/s	4 m/s	5 m/s	6 m/s	7 m/s
S0	0	0	0.010	0.027	0.030	0.046	0.057
S1	0	0	0.046	0.084	0.134	0.295	0.384
S2	0	0.013	0.116	0.231	0.268	0.432	0.510
S3	0.035	0.039	0.268	0.376	0.493	0.605	1.037
S4	0.071	0.110	0.368	0.556	0.739	0.973	1.354
S5	0.103	0.151	0.501	0.696	0.924	1.664	2.152

Note: The power values were calculated from the corresponding mean RMS voltage values under R_L=1 MΩ. All entries are fixed-load outputs and should not be interpreted as independently optimised maximum power points for the individual prototypes.

The same conclusion is supported by the power data in **Table 3**. As tail length increases, the fixed-load power output grows monotonically across the tested range. At 7 m/s, S5 provides a fixed-load power output of 2.152 mW, compared with 0.057 mW for S0 under the same R_L=1 MΩ condition. Even at lower wind speeds, the difference remains substantial. For example, S5 already satisfies the defined voltage-response-based cut-in criterion at 1 m/s, whereas S0 remains at a low-amplitude, noise-dominated level under the same wind condition. These results indicate that tail extension strengthens not only the output after response development, but also the practical usability of the harvester in the low-speed regime.

It should be noted that **Table 3** reports the power output under a fixed external resistance of R_L=1 MΩ. This load condition was selected based on the previously reported load-resistance optimisation of a related curved-plate piezoelectric wind energy harvester, in which the optimal resistance was approximately 820 kΩ and varied only weakly with wind speed [35]. However, that previously reported value was used only as a reference and does not establish the optimum resistance of the present prototypes. Because a complete load-resistance sweep was not performed for each prototype, the electrical comparison is intentionally reported under the same fixed-load condition to ensure consistency among the S-series geometries. The resulting power values should therefore be interpreted as fixed-load outputs rather than independently measured maximum power points.

Taken together, the S-series results indicate that tail length is the primary geometric variable governing the low-speed response defined in this paper. Increasing tail length shifts the defined voltage-response-based cut-in threshold to lower wind speeds and produces larger lift, voltage and fixed-load power output once oscillation is established. The broad wind-speed response, progressive amplitude growth and systematic dependence on tail length support the interpretation of the subsequent regime as galloping-dominated, rather than a purely noise-dominated perturbation or an isolated VIV-type lock-in response.

At the same time, the tail-length effect should not be interpreted as purely aerodynamic. The repeated mass measurements show that tail extension increases the physical mass of the bluff body, while the CAD calculations indicate a downstream shift of the centre of gravity. The experiments also show a general reduction in vibration frequency as the tail length increases. Taken together, these observations support a structural-dynamic contribution to the overall response, although the aerodynamic and inertial effects were not independently quantified. This frequency reduction has practical implications for energy harvesting because a lower vibration frequency means fewer strain cycles per unit time. In the present S-series models, however, the lower frequency is accompanied by much larger lift response, beam deformation and RMS voltage. Therefore, within the tested tail-length range, the benefit of larger aerodynamic forcing and strain amplitude outweighs the disadvantage of the reduced vibration frequency.

Nevertheless, this result should not be interpreted as meaning that an indefinitely longer tail would always be preferable. Further tail extension may continue to reduce the characteristic response frequency and increase the inertial burden of the bluff-body–beam system. Beyond a certain range, the gain in strain amplitude may no longer compensate for the reduction in cycle rate and the increase in structural loading. Therefore, S5 should be regarded as the best-performing model within the tested parameter range, rather than as proof that the longest possible tail is universally optimal.

4.4 Effect of curved-section thickness

Compared with tail addition and tail length, curved-section thickness is treated here as a secondary geometric factor. The purpose of the R-series comparison is therefore not to redefine the main contribution of the study, but to examine whether the aerodynamic response can be further refined by modifying the thickness of the curved section while maintaining similar tail-length ratios. For this reason, R1 and R2 were compared with S4 and S5, respectively.

As shown in Supplementary **Fig. S5**, both R-series models produce higher RMS voltage than their corresponding S-series counterparts over the tested wind-speed range. This result suggests that reducing the curved-section thickness may improve the aerodynamic sensitivity of the reverse-C-with-tail geometry and enhance the resulting electrical output. However, this comparison should be interpreted as a preliminary indication rather than as a fully decoupled parametric conclusion. Only two thin-section R-series prototypes, R1 and R2, were successfully fabricated, corresponding to tail lengths of 30 mm and 40 mm, respectively. Therefore, the present R-series does not provide a complete thickness sweep over the full tail-length range.

One possible aerodynamic interpretation is that curved-section thickness influences shear-layer separation and the tendency for local reattachment near the rear part of the body. A thinner section may preserve a sharper separated-flow pattern, whereas a thicker section may allow greater local flow recovery along the surface. However, this interpretation remains qualitative. The present R-series did not include a complete thickness-controlled CFD study, and reattachment location, pressure difference and recirculation length were not extracted as scalar metrics. Therefore, the higher voltage of R1 and R2 cannot be attributed uniquely to a quantified suppression of reattachment; it should be regarded as preliminary evidence of a coupled geometric and structural effect. This interpretation is consistent with the wake-modification mechanism discussed in Section 3, but it remains qualitative because the R-series was not supported by a complete set of thickness-controlled CFD and experimental cases.

The R-series also reveals an important manufacturability and robustness constraint. Several intended thin-section prototypes could not be printed successfully because the 0.5 mm curved section was mechanically fragile. In addition, reducing the curved-section thickness may influence not only the local flow separation behaviour, but also the structural stiffness, durability and vibration characteristics of the bluff body. Therefore, the observed improvement cannot be attributed to aerodynamic thickness effects alone without qualification.

For these reasons, curved-section thickness is treated in this study as a secondary refinement parameter rather than as a primary source of novelty. The main conclusion of the paper remains based on the T-series and S-series results, which demonstrate the role of tail addition and tail length in reducing the voltage-response-based cut-in threshold and improving fixed-load electrical output. The R-series provides useful preliminary evidence that local geometric refinement may further improve the already effective reverse-C-with-tail design, but future work should examine thickness and tail length in a fully factorial manner. This could be achieved through improved manufacturing methods, such as higher-resolution printing, optimised printing orientation, reinforced polymer materials or thin metallic inserts, so that thinner curved sections can be tested without compromising structural reliability.

4.5 Overall interpretation of the experimental results

Across all three experimental series, a clear hierarchy of effects emerges. First, the T-series demonstrates that the tail itself is the decisive geometric feature that promotes low-speed electrical response and strengthens the subsequent galloping-dominated response. Compared with the tailless configuration, the tailed model consistently exhibits higher lift and much larger RMS voltage, confirming that the tail fundamentally changes the harvester behaviour rather than merely providing a minor improvement.

Second, the S-series shows that tail length is the dominant parameter controlling how strongly this tail-enabled advantage develops. As tail length increases, the lift response becomes stronger, the voltage output rises monotonically, and the defined voltage-response-based cut-in threshold shifts downward. The longer-tail models begin to generate measurable electrical response at approximately 1–2 m/s, whereas the tailless baseline remains largely noise-dominated in this low-speed range. This is the most important experimental evidence supporting the central claim of the paper: the proposed reverse-C-with-tail concept shifts the voltage-response-based cut-in threshold to a substantially lower wind-speed range.

Third, the R-series suggests that thinner curved sections may enhance electrical output. A possible explanation involves altered separation and reattachment behaviour, but this interpretation remains qualitative because no scalar reattachment, pressure-difference or recirculation-length metric was obtained for the thickness comparison.

Another important outcome of the experiments is that improved low-speed accessibility does not come at the expense of useful performance at higher wind speeds. The longer-tail configurations not only respond earlier, but also continue to deliver higher voltage and fixed-load power output under the common R_L=1 MΩ condition as wind speed increases. This means that the present design does not merely shift the defined electrical cut-in threshold downward while sacrificing the subsequent operating range. Instead, it achieves both earlier electrical activation and stronger steady-state harvesting capability.

At the same time, the experiments also reveal a trade-off that should be acknowledged explicitly. While longer tails improve cut-in behaviour and output magnitude, they also tend to reduce vibration frequency. This implies that future optimisation should not aim only at maximising tail length, but rather at balancing amplitude growth, frequency response, structural integrity, and manufacturability. Even so, this trade-off does not weaken the main conclusion of the present section. On the contrary, it reinforces the idea that the tail is a physically meaningful design lever whose influence extends across multiple aspects of harvester performance.

A further comparison between the experimental measurements and the simplified CFD predictions is provided in Supplementary **Fig. S6**. The figure plots the ratio of experimentally measured lift force to CFD-predicted lift force for the S-series models over the investigated wind-speed range. For most configurations (S0–S4), this ratio increases with wind speed and becomes more clearly greater than unity at higher velocities, indicating that the simplified two-dimensional fixed-body CFD tends to underestimate the transverse aerodynamic loading observed in the experiments. This difference is physically reasonable because the CFD model neglects spanwise flow, end effects, and motion-induced fluid–structure interaction, whereas the experiments capture a dynamically coupled response in which structural motion can amplify the effective aerodynamic force.

Supplementary **Figure S6** also suggests that the S5 configuration behaves somewhat differently from the shorter-tail cases. Its experimental-to-CFD ratio remains comparatively stable across the velocity range, whereas the other configurations show a more evident upward trend. The comparatively stable experimental-to-CFD ratio of S5 indicates that the discrepancy between the fixed-body estimate and the measured coupled response is less sensitive to wind speed for this configuration. However, this ratio alone does not demonstrate that the wake is more organised, because no independent scalar metric of wake organisation was extracted. Any interpretation linking the stable ratio to more regular flow behaviour should therefore be regarded as tentative. Supplementary **Figure S6** is used primarily to characterise the configuration-dependent discrepancy between the simplified CFD and the experiment, rather than to establish an additional wake mechanism. This comparison therefore does not weaken the role of the CFD analysis presented in Section 3; rather, it clarifies that the preliminary CFD should be understood as a qualitative aerodynamic tool, while the experiments provide the primary evidence for the actual coupled response.

In summary, the experimental results support a consistent interpretation: the tail is the primary enabling feature for low-speed electrical activation and subsequent galloping-dominated response, tail length controls the strength of this low-speed advantage and the subsequent output growth, and curved-section thickness provides secondary fine-tuning of the aerodynamic response. This hierarchy allows the main novelty of the manuscript to be stated more clearly: the contribution is not simply a generic shape modification, but an experimentally validated ultra-low-cut-in design strategy for galloping-based piezoelectric energy harvesting.

5. Reduced-Order Modelling and Trend Interpretation

5.1 Purpose of the reduced-order model

Although the wind tunnel experiments provide the primary evidence for the performance of the proposed harvester, a reduced-order electromechanical model is useful for interpreting the observed response trends in a compact and physically transparent form. The model is not intended to reproduce the detailed unsteady flow field, resolve full fluid–structure interaction or replace the experimental measurements. Instead, it is used as an interpretive framework to examine whether the main RMS-voltage trends of the S-series models can be represented through a small number of equivalent aerodynamic parameters within a standard galloping-based piezoelectric harvesting formulation.

This distinction is important for interpreting the modelling results. In this manuscript, the low-speed electrical response and voltage/power enhancement of the reverse-C-with-tail geometry are established primarily by wind tunnel experiments, while the preliminary CFD analysis provides aerodynamic support for the role of tail-guided wake modification. The reduced-order model is therefore introduced after the experimental trends have been identified.

Its role is to reproduce the measured RMS-voltage trends at the curve level and to interpret how tail extension is reflected in the fitted aerodynamic coefficients A_1 and A_3. These coefficients were identified by fitting the same experimental mean RMS-voltage dataset used in the subsequent curve comparison. The resulting curves therefore represent an in-sample reproduction of the measured trends. Accordingly, the model is treated as an interpretive framework rather than as an independently validated aerodynamic model.

5.2 Governing equations of the coupled system

The modelling framework adopted in this work follows the general principle of galloping-based piezoelectric energy harvesting, in which the aerodynamic, mechanical, and electrical subsystems are described in coupled form. The aerodynamic transverse force acting on the bluff body is expressed by a low-order polynomial expansion that relates the aerodynamic forcing to the motion-induced velocity. In simplified form, the aerodynamic force is written as Eq. (1) [45]:

$$F_a = \frac{1}{2}\rho U^2 DL\left[A_1\left(\frac{\dot{\eta}}{U}\right) - A_3\left(\frac{\dot{\eta}}{U}\right)^3\right]$$

Equation (1)

where F_a is the instantaneous aerodynamic force, ρ the air density, U the wind velocity, D and L denote the characteristic geometric dimensions of the bluff body. The coefficients A_1 and A_3 are geometry-dependent aerodynamic parameters that reflect the effective destabilising and nonlinear characteristics of the flow-structure interaction. In the context of the present study, these coefficients are expected to vary with tail length and curved-section geometry, and thus provide a compact way to represent the aerodynamic influence of the different prototype configurations.

The mechanical response of the cantilever-piezoelectric system is then described by the coupled transverse vibration equation:

$$M\ddot{\eta} + C\dot{\eta} + k\eta - \Theta U_p = F_a$$

Equation (2)

The corresponding electrical circuit equation is:

$$C_e\dot{U}_p + \frac{U_p}{R_L} + \Theta\dot{\eta} = 0$$

Equation (3)

where M, C, and k denote the effective mass, damping, and stiffness of the system, Θ is the electromechanical coupling coefficient, U_p is the output voltage across the external load R_L, and C_e represents the equivalent capacitance of the piezoelectric sheet.

Substituting Eq. (1) into Eq. (2) and solving using the multiscale method yields an approximate analytical solution for the steady-state amplitude of displacement and voltage [46]:

$$\frac{|\eta|}{\eta_0} = \frac{|U_p|}{U_{p0}} = 2\sqrt{\frac{U^*(A_1U^* - 1)}{3A_3}}$$

Equation (4)

where U^* is the dimensionless wind velocity defined below, and η_0, U_{p0} are the corresponding reference amplitudes. Eq. (4) provides the modelled voltage curves used for trend-level comparison with the experimental data.

For clarity, several dimensionless quantities are introduced:

$$\lambda = \frac{\rho D L^2}{4M} \quad , \quad \alpha = \frac{1}{R_L C_e \omega_n} \quad , \quad \xi = \frac{\Theta^2}{M 2_\omega^n C_e}$$

Equation (5)

where $\omega_n = \sqrt{k/M}$ is the natural frequency of the system. The parameters λ, α, and ξ represent the flow-to-mass ratio, the electrical time-constant ratio, and the non-dimensional coupling coefficient, respectively. These quantities establish the link between structural characteristics, electrical loading, and aerodynamic effects. By assigning the fitted values of A_1 and A_3 to each tested geometry, a modelled voltage curve can be generated using Eq. (4).

5.3 Model Parameters and Identification of A_1 and A_3

To construct the modelled voltage curves obtained from Eq. (4), the principal mechanical and electromechanical parameters of the system were determined from experimental measurements and material data, as summarised in Supplementary **Table S3.**

Using these parameters, the aerodynamic coefficients A_1 and A_3 were identified separately for each S-series model by fitting the modelled RMS-voltage curve derived from Eq. (4) to the corresponding experimentally measured mean RMS-voltage data. In the fitting procedure, the mechanical and electromechanical parameters listed in Supplementary **Table S3** were kept fixed, while A_1 and A_3 were adjusted to reduce the residual difference between the calculated and measured RMS voltages over the tested wind-speed range. The fitted values are summarised in Supplementary **Table S4**, and the corresponding modelled RMS-voltage curves are presented in Supplementary **Fig. S7**.

It should be noted that A_1 and A_3 are equivalent aerodynamic coefficients identified at the system level. They should not be interpreted as independently measured aerodynamic constants of the bluff body. Instead, they provide a compact representation of the combined aerodynamic and structural-dynamic influence of each prototype configuration within the reduced-order formulation. The fitted A_1 value increases from S0 to S5, indicating that longer tails are associated with a stronger effective destabilising aerodynamic contribution. By contrast, the fitted A_3 values mainly represent nonlinear saturation effects and should be interpreted more cautiously, because they may also absorb unmodelled effects such as amplitude-dependent damping, startup instability and imperfect flow–structure coupling.

5.4 Modelled–Experimental Trend Comparison and Discussion

Using the parameter set in Supplementary **Table S3** and the fitted aerodynamic coefficients in Supplementary **Table S4**, the modelled RMS voltage curves were obtained for the S-series models, as shown in Supplementary **Fig. S7**. Overall, the reduced-order model captures the main curve-level trends observed in the experiments. In both the modelled and measured responses, the RMS voltage increases with wind speed, and the longer-tail models generally produce higher voltage than the shorter-tail and tailless configurations. The modelled curves also reproduce the main fitted trend that the electrical response shifts toward lower wind speeds as tail length increases.

For example, the modelled S0 curve remains weak at low wind speeds, whereas the S5 curve shows an earlier and stronger voltage response and reaches a voltage level close to the measured value at 7 m/s. This agreement indicates that the reduced-order formulation can reproduce the main geometry-dependent voltage trend after coefficient identification. It does not provide an independent validation of the cut-in wind speed, because A_1 and A_3 were fitted using the same experimental RMS-voltage dataset included in the curve comparison.

The relative spacing among the model curves is also consistent with the measured trend. In both the modelled and experimental results, the performance gap between intermediate and long-tail cases becomes smaller as tail length continues to increase, indicating a tendency toward diminishing incremental gain at larger tail-to-diameter ratios. This behaviour is consistent with the aerodynamic interpretation developed earlier in the paper: once the tail is sufficiently long for the contour fields to show a qualitatively more extended recirculating-flow pattern and a more pronounced pressure contrast, further extension is associated with a smaller incremental increase in the fitted voltage response. The flow-field interpretation remains qualitative because neither recirculation length nor pressure difference was extracted as a scalar metric.

Despite this generally consistent trend, deviations between the modelled and measured curves remain, especially near the low- and high-speed ends of the investigated range. In the low-speed region, the reduced-order model assumes an idealised steady oscillatory response, whereas the real harvester near cut-in can be affected by startup friction, signal instability and unsteady local flow variation. At higher wind speeds, the measured voltage may deviate from the fitted curve because of increased material damping, measurement limitations, possible piezoelectric response saturation and amplitude-dependent nonlinearities. In addition, the model treats damping and coupling parameters in an equivalent and simplified manner and cannot resolve all nonlinear flow–structure interaction effects.

Because all available S-series voltage data were used for coefficient identification, an independent validation dataset was not available in the present study. Therefore, the model is not presented as an independently validated or generally applicable design tool. Its value lies in providing an interpretable reduced-order description of the measured trends and in showing that the effect of tail length can be represented through systematic changes in the fitted equivalent aerodynamic coefficients. The modelling results are thus used together with the CFD interpretation and wind tunnel measurements to support the physical explanation of the reverse-C-with-tail design, rather than to replace direct experimental validation.

6. Limitations and Future Work

The present study was designed to clarify the aerodynamic role of a reverse-C-with-tail bluff body in enabling low-speed voltage-response-based cut-in and enhancing the subsequent galloping-dominated piezoelectric energy harvesting response. Although the combined CFD, experimental and reduced-order modelling results provide consistent support for the proposed design concept, several limitations should be acknowledged.

One limitation concerns the controlled wind tunnel conditions used in the experiments. This environment is appropriate for isolating the effects of tail addition, tail length and curved-section thickness, but it does not fully represent the variability of real atmospheric flow. In practical deployment, the harvester may be exposed to turbulence, gusts, intermittent flow, changing wind direction and installation-dependent inflow angles. These factors may affect both the voltage-response-based cut-in condition and the stability of the subsequent galloping-dominated response. In particular, the reverse-C-with-tail geometry is expected to be directionally sensitive because its aerodynamic advantage depends on the relative orientation between the incoming flow, the curved cavity and the tail. Therefore, the present results should be interpreted as a controlled demonstration of the design principle rather than a complete evaluation of field performance.

A second limitation concerns environmental durability and outdoor deployment. The present prototypes were fabricated from PLA and were not designed as weather-resistant devices. Rain, humidity, dust accumulation and temperature variation may change the surface condition of the bluff body, affect the stiffness and durability of the printed structure, and influence the bonding reliability between the piezoelectric patch and the cantilever beam. Long-term cyclic loading may also lead to fatigue in the cantilever, degradation of the adhesive layer, piezoelectric depolarisation or cracking, and loosening of the mechanical connection between the bluff body and the beam. In addition, practical outdoor operation would require suitable packaging to protect the piezoelectric patch, electrodes and electrical connections without excessively increasing stiffness or suppressing the desired vibration response. These issues were beyond the scope of the present wind tunnel study and should be evaluated in future field-oriented tests.

Another limitation concerns the preliminary scope of the CFD analysis. The simulations were performed in a two-dimensional fixed-body framework and were used mainly to provide qualitative aerodynamic insight into wake development, recirculation, and pressure asymmetry. As a result, they do not account for three-dimensional flow structures, spanwise effects, end effects, or motion-induced feedback between the vibrating structure and the surrounding flow. These limitations mean that the numerical results should be interpreted as semi-quantitative mechanistic support for the proposed design rather than as a direct quantitative reproduction of the experimental response. Higher-fidelity fluid-structure interaction analysis would be valuable in future work to resolve these effects more completely.

The reduced-order electromechanical model is also limited in its scope for independent generalisation. In the present study, the model was introduced primarily to reproduce the measured voltage trends and to interpret the influence of geometric variation through equivalent aerodynamic coefficients. Because A_1 and A_3 were identified by fitting the same experimental RMS-voltage dataset used for the modelled–experimental curve comparison, the formulation should be regarded as an interpretive trend-reproduction framework rather than as an independently validated aerodynamic model. It captures the main fitted trend that longer tails are associated with earlier and stronger response, but it does not resolve all nonlinearities related to startup behaviour, amplitude-dependent damping or detailed unsteady flow effects.

The R-series comparison also reveals a manufacturability-related limitation. Although the two successful R-series prototypes suggest that thinner curved sections can improve electrical output, the fabrication results also reveal a practical trade-off between aerodynamic sensitivity and structural robustness. Only two of the intended thin-curved prototypes could be manufactured successfully, indicating that excessively thin geometries may be difficult to fabricate and may face limitations in long-term durability. For practical device development, geometric optimisation must therefore consider not only aerodynamic performance but also manufacturability and service reliability.

Finally, the aerodynamic and structural-dynamic effects of tail extension were not fully decoupled. Although the S-series controlled the reverse-C body, material, frontal width, inner diameter and mounting scheme, tail extension increased the physically measured bluff-body mass and shifted the CAD-derived centre-of-gravity position downstream, while the measured coupled vibration frequency generally decreased. The repeated mass readings were identical within the 0.1 g resolution of the balance, but the CAD-derived centre-of-gravity positions were not independently verified through physical balancing measurements and may be affected by printing tolerances and variations in the actual material distribution. Future work should combine physical centre-of-gravity measurements, mass-balanced bluff-body designs, independent modal testing and aeroelastic simulations to isolate the relative contributions of wake modification and structural dynamics.

Based on these limitations, several directions for future work can be identified. One important extension is to perform higher-fidelity three-dimensional fluid–structure interaction simulations to capture the motion-dependent aerodynamic behaviour of the reverse-C-with-tail configuration more accurately. Another is to test the harvester under more realistic inflow conditions, including turbulent flow, gusts, variable wind direction and intermittent low-speed wind, so that its low-speed accessibility and response stability can be evaluated beyond controlled tunnel conditions. Future studies should also examine environmental durability, including rain and humidity exposure, temperature variation, dust accumulation, PLA ageing, piezoelectric patch bonding reliability, electrode protection and long-term fatigue under repeated oscillation.

Further parametric optimisation should balance tail geometry, curved-section thickness, structural mass distribution, cut-in wind speed, voltage output, vibration frequency, structural robustness and fabrication feasibility. Finally, the harvester should be integrated with rectification, power-management, energy-storage and protective packaging systems to assess its applicability as a practical low-speed wind-powered sensing unit.

7. Conclusion

This study proposed a reverse-C-with-tail bluff-body piezoelectric harvester for low-speed wind energy conversion and demonstrated that its main advantage lies in enabling a repeatable voltage-response-based cut-in at approximately 1 m/s, followed by a galloping-dominated response over the subsequent tested wind-speed range. The proposed geometry should not be regarded simply as another bluff-body shape variation. Instead, the reverse-C cavity and rear tail are interpreted as an integrated wake-guiding structure. The fixed-body CFD provides quantitative evidence of stronger lift-coefficient fluctuations for the tailed geometry, while the pressure contours and streamlines qualitatively suggest a more extended recirculating-flow pattern, less immediate shear-layer reattachment and a more pronounced upper–lower pressure contrast. Because pressure difference, recirculation length and vortex-shedding frequency were not extracted as scalar metrics, these flow-field features are presented as qualitative mechanistic observations rather than quantitative conclusions.

Wind tunnel experiments confirmed the aerodynamic and electrical advantages of this design. The T-series showed that tail addition fundamentally strengthens the coupled response of the harvester. The

S-series further demonstrated that tail length is the primary geometric parameter controlling the low-speed advantage: longer tails produce stronger lift responses and higher RMS voltages. Under the common fixed-load condition of R_L=1 MΩ, S5 reaches a power output of 2.152 mW at 7 m/s; this value is a fixed-load result rather than an independently optimised maximum power point. The longest-tail configuration also satisfies the adopted voltage-response-based cut-in criterion at approximately 1 m/s. The R-series provided preliminary evidence that reducing the curved-section thickness may further improve electrical output; however, because only two thin-section prototypes were successfully fabricated and tested, this effect should be regarded as a secondary refinement rather than a fully isolated thickness-effect conclusion.

The reduced-order electromechanical model reproduced the main RMS-voltage trends after coefficient identification and supported the interpretation that tail extension systematically modifies the effective aerodynamic behaviour of the harvester. Because the aerodynamic coefficients were fitted using the same experimental voltage data included in the curve comparison, the model should be interpreted as a trend-reproduction and interpretive framework rather than as an independently validated design tool. Taken together, the CFD analysis, wind tunnel experiments and reduced-order modelling consistently support the main contribution of this work: an experimentally validated ultra-low-cut-in design strategy for galloping-based piezoelectric energy harvesting based on integrated reverse-C cavity and tail-guided wake modification.

From a practical perspective, the proposed design is most relevant to low-power sensing and monitoring scenarios where weak or intermittent airflow is available but conventional small wind harvesters may remain inactive, such as ventilation ducts, building-integrated airflow monitoring, agricultural or environmental sensing stations and distributed industrial monitoring systems. The device is not intended to replace conventional wind turbines or supply high-power loads; rather, its significance lies in improving the accessibility of piezoelectric wind harvesting under weak-flow conditions. Future development should focus on optimizing the tail geometry together with structural mass distribution, improving durability and packaging, testing under turbulent and directionally varying wind conditions, and integrating rectification, energy-storage and power-management circuits to evaluate the feasibility of a robust low-speed wind-powered sensing unit.

Acknowledgements

This work was supported by National Key R&D Program of China (No. 2023YFB4203401).

References

[1] M. Y. Gao, P. Wang, Y. Cao, R. Chen, and C. Liu, "A rail-borne piezoelectric transducer for energy harvesting of railway vibration," *Journal of Vibroengineering*, vol. 18, no. 7, pp. 4647–4663, 2016, doi: 10.21595/jve.2016.16938.

[2] C. Chen, A. Sharafi, and J. Q. Sun, "A high density piezoelectric energy harvesting device from highway traffic – Design analysis and laboratory validation," *Appl. Energy*, vol. 269, Jul. 2020, doi: 10.1016/j.apenergy.2020.115073.

[3] Z. Xie, C. A. Kitio Kwuimy, Z. Wang, and W. Huang, "A piezoelectric energy harvester for broadband rotational excitation using buckled beam," *AIP Adv.*, vol. 8, no. 1, Jan. 2018, doi: 10.1063/1.5018077.

[4] Z. Xie, J. Xiong, D. Zhang, T. Wang, Y. Shao, and W. Huang, "Design and experimental investigation of a piezoelectric rotation energy harvester using bistable and frequency up-conversion mechanisms," *Applied Sciences (Switzerland)*, vol. 8, no. 9, Aug. 2018, doi: 10.3390/app8091418.

[5] X. Cui, M. Teng, and J. Hu, "PSPICE-Based Analyses of the Vibration Energy Harvester System with Multiple Piezoelectric Units," *Canadian Journal of Electrical and Computer Engineering*, vol. 38, no. 3, pp. 246–250, Jun. 2015, doi: 10.1109/CJECE.2015.2431312.

[6] Z. Wang, L. Hou, J. He, M. Yao, and T. Yang, "Dual-Functional Triboelectric-Electromagnetic hybrid nanogenerator for Simultaneous Vibration Energy Harvesting and Vibration Suppression," *Nano Energy*, p. 111277, Sep. 2025, doi: 10.1016/j.nanoen.2025.111277.

[7] J. Pan *et al.*, "A phase-synchronized triboelectric-assisted electromagnetic energy harvesting system for omnidirectional low-frequency wave energy," *Energy*, vol. 328, Aug. 2025, doi: 10.1016/j.energy.2025.136529.

[8] Z. Li, T. Zhao, B. Niu, Y. Ma, and C. Hu, "A hydrokinetic Turbine-Based Triboelectric-Electromagnetic hybrid generator for ocean current energy harvesting," *Energy Convers. Manag.*, vol. 326, Feb. 2025, doi: 10.1016/j.enconman.2024.119473.

[9] J. Teng, Z. Cao, C. Ren, J. Xu, X. Guo, and X. Ye, "Efficient energy harvesting from broadband low-frequency vibrations via 3D-interdigital electrostatic generator," *Appl. Energy*, vol. 388, Jun. 2025, doi: 10.1016/j.apenergy.2025.125701.

[10] M. A. Ben Hassena, H. Samaali, H. M. Ouakad, and F. Najar, "2D electrostatic energy harvesting device using a single shallow arched microbeam," *Int. J. Non. Linear. Mech.*, vol. 132, Jun. 2021, doi: 10.1016/j.ijnonlinmec.2021.103700.

[11] C. Li *et al.*, "Droplet-piezoelectric nanogenerators for simultaneous harvesting of droplet electrostatic and mechanical energy," *Chemical Engineering Journal*, vol. 518, Aug. 2025, doi: 10.1016/j.cej.2025.164565.

[12] O. Hussein, W. K．S．Al-jumaili, F. F．Mustafa, E. Al−Ali, and M. A. Mohammed, "Hybrid energy harvesting using piezoelectric footsteps and solar panels to ensure clarity," *Results in Engineering*, vol. 26, Jun. 2025, doi: 10.1016/j.rineng.2025.104945.

[13] M. Rezaeisaray, M. El Gowini, D. Sameoto, D. Raboud, and W. Moussa, "Low frequency piezoelectric energy harvesting at multi vibration mode shapes," *Sens. Actuators A Phys.*, vol. 228, pp. 104–111, Jun. 2015, doi: 10.1016/j.sna.2015.02.036.

[14] A. I. Sadaf, M. Mohiuddin, R. Ahmed, D. Meade, K. Akter, and H. Ahmed, "Harnessing vibrations: A review on structural architecture and design ideology of the cantilever beam based piezoelectric energy harvesters," *Appl. Energy*, vol. 396, Oct. 2025, doi: 10.1016/j.apenergy.2025.126286.

[15] R. Bolt, M. Magno, T. Burger, A. Romani, and L. Benini, "Kinetic AC/DC Converter for Electromagnetic Energy Harvesting in Autonomous Wearable Devices," *IEEE Transactions on Circuits and Systems II: Express Briefs*, vol. 64, no. 12, pp. 1422–1426, Dec. 2017, doi: 10.1109/TCSII.2017.2768391.

[16] Z. Lai *et al.*, "A hybrid piezo-dielectric wind energy harvester for high-performance vortex-induced vibration energy harvesting," *Mech. Syst. Signal Process.*, vol. 150, Mar. 2021, doi: 10.1016/j.ymssp.2020.107212.

[17] L. Ding, Q. Zou, L. Zhang, and H. Wang, "Research on Flow-Induced Vibration and Energy Harvesting of Three Circular Cylinders with Roughness Strips in Tandem," *Energies (Basel).*, vol. 11, no. 11, Nov. 2018, doi: 10.3390/en11112977.

[18] S. Zhou and J. Wang, "Dual serial vortex-induced energy harvesting system for enhanced energy harvesting," *AIP Adv.*, vol. 8, no. 7, Jul. 2018, doi: 10.1063/1.5038884.

[19] H. L. Dai, A. Abdelkefi, Y. Yang, and L. Wang, "Orientation of bluff body for designing efficient energy harvesters from vortex-induced vibrations," *Appl. Phys. Lett.*, vol. 108, no. 5, pp. 1–6, 2016, doi: 10.1063/1.4941546.

[20] J. Jia, X. Shan, D. Upadrashta, T. Xie, Y. Yang, and R. Song, "An asymmetric bending-torsional piezoelectric energy harvester at low wind speed," *Energy*, vol. 198, May 2020, doi: 10.1016/j.energy.2020.117287.

[21] J. Wang *et al.*, "Hybrid wind energy scavenging by coupling vortex-induced vibrations and galloping," *Energy Convers. Manag.*, vol. 213, Jun. 2020, doi: 10.1016/j.enconman.2020.112835.

[22] J. Song, G. Hu, K. T. Tse, S. W. Li, and K. C. S. Kwok, "Performance of a circular cylinder piezoelectric wind energy harvester fitted with a splitter plate," *Appl. Phys. Lett.*, vol. 111, no. 22, Nov. 2017, doi: 10.1063/1.5008918.

[23] F. Ewere, G. Wang, and B. Cain, "Experimental investigation of galloping piezoelectric energy harvesters with square bluff bodies," *Smart Mater Struct*, vol. 23(10), 2014, doi: 10.1088/0964-1726/23/10/104012.

[24] Y. Zhang, C. Ma, J. Li, and C. Pei, "Self-excited force characteristics and flow mechanisms of a 5:1 rectangular cylinder in torsional vortex-induced vibration and flutter," *Ocean Engineering*, vol. 312, Nov. 2024, doi: 10.1016/j.oceaneng.2024.119027.

[25] H. Tian, X. Shan, H. Wang, X. Li, Y. Su, and J. Wang, "Enhanced piezoelectric energy harvesting performance using trailing-edge flap," *Ocean Engineering*, vol. 285, Oct. 2023, doi: 10.1016/j.oceaneng.2023.115443.

[26] M. Bashir, P. Rajendran, and S. A. Khan, "Energy Harvesting from Aerodynamic Instabilities: Current prospect and Future Trends," in *IOP Conference Series: Materials Science and Engineering*, Institute of Physics Publishing, Jan. 2018. doi: 10.1088/1757-899X/290/1/012054.

[27] Z. Yan, G. Shi, J. Zhou, L. Wang, L. Zuo, and T. Tan, "Wind piezoelectric energy

harvesting enhanced by elastic-interfered wake-induced vibration," *Energy Convers. Manag.*, vol. 249, Dec. 2021, doi: 10.1016/j.enconman.2021.114820.

[28] J. F. Derakhshandeh, M. Arjomandi, B. Dally, and B. Cazzolato, "The effect of arrangement of two circular cylinders on the maximum efficiency of Vortex-Induced Vibration power using a Scale-Adaptive Simulation model," *J. Fluids Struct.*, vol. 49, pp. 654–666, 2014, doi: 10.1016/j.jfluidstructs.2014.06.005.

[29] M. Gong and B. Dally, "A review of flow-induced vibration in wind and oceanic flow: Mechanisms, applications, optimizations, and challenges," May 01, 2025, *Elsevier Ltd*. doi: 10.1016/j.oceaneng.2025.120748.

[30] D. Zhao, X. Hu, T. Tan, Z. Yan, and W. Zhang, "Piezoelectric galloping energy harvesting enhanced by topological equivalent aerodynamic design," *Energy Convers. Manag.*, vol. 222, Oct. 2020, doi: 10.1016/j.enconman.2020.113260.

[31] N. Shao *et al.*, "Experimental investigation of flow-induced motion and energy conversion of a T-section prism," *Energies (Basel).*, vol. 11, no. 8, Aug. 2018, doi: 10.3390/en11082035.

[32] F. R. Liu, H. X. Zou, W. M. Zhang, Z. K. Peng, and G. Meng, "Y-type three-blade bluff body for wind energy harvesting," *Appl. Phys. Lett.*, vol. 112, no. 23, Jun. 2018, doi: 10.1063/1.5029415.

[33] A. Abdelkefi, M. R. Hajj, and A. H. Nayfeh, "Power harvesting from transverse galloping of square cylinder," *Nonlinear Dyn.*, vol. 70, no. 2, pp. 1355–1363, Oct. 2012, doi: 10.1007/s11071-012-0538-4.

[34] K. Zhao, Q. Zhang, and W. Wang, "Optimization of Galloping Piezoelectric Energy Harvester with V-Shaped Groove in Low Wind Speed," *Energies (Basel).*, vol. 12, no. 24, p. 4619, Dec. 2019, doi: 10.3390/en12244619.

[35] C. F. Zhou, H. X. Zou, K. X. Wei, and J. G. Liu, "Enhanced performance of piezoelectric wind energy harvester by a curved plate," *Smart Mater. Struct.*, vol. 28, no. 12, Nov. 2019, doi: 10.1088/1361-665X/ab525a.

[36] J. Zheng, Z. Li, and H. Zhang, "Low-Wind-Speed Galloping Wind Energy Harvester Based on a W-Shaped Bluff Body," *Energies (Basel).*, vol. 17, no. 4, p. 958, Feb. 2024, doi: 10.3390/en17040958.

[37] W. Du, L. Liang, Z. Zhou, W. Qin, H. Huang, and D. Cao, "Enhancing piezoelectric energy harvesting from the flow-induced vibration of an apple-shaped bluff body based on topology optimization," *Energy*, vol. 307, p. 132667, Oct. 2024, doi: 10.1016/j.energy.2024.132667.

[38] J. Song, G. Hu, L. Zou, and T. Shi, "Aerodynamic shape optimization of bluff body for galloping-based wind energy harvester by the class function/shape function transformation technique," *J. Fluids Struct.*, vol. 123, p. 104001, Nov. 2023, doi: 10.1016/j.jfluidstructs.2023.104001.

[39] F.-R. Liu *et al.*, "Performance enhancement of wind energy harvester utilizing wake flow induced by double upstream flat-plates," *Appl. Energy*, vol. 257, p. 114034, Jan. 2020, doi: 10.1016/j.apenergy.2019.114034.

[40] L. B. Zhang, H. L. Dai, A. Abdelkefi, and L. Wang, "Experimental investigation of aerodynamic energy harvester with different interference cylinder cross-sections," *Energy*, vol. 167, pp. 970–981, Jan. 2019, doi: 10.1016/j.energy.2018.11.059.

[41] H.-T. Li, H. Ren, F. Cao, and W.-Y. Qin, “Improving the galloping energy harvesting performance with magnetic coupling,” *Int. J. Mech. Sci.*, vol. 237, p. 107785, Jan. 2023, doi: 10.1016/j.ijmecsci.2022.107785.

[42] Q. Wang *et al.*, “A synergetic hybrid mechanism of piezoelectric and triboelectric for galloping wind energy harvesting,” *Appl. Phys. Lett.*, vol. 117, no. 4, Jul. 2020, doi: 10.1063/5.0014484.

[43] X. Li, C. Bi, Z. Li, B. Liu, T. Wang, and S. Zhang, “A Piezoelectric and Electromagnetic Hybrid Galloping Energy Harvester with the Magnet Embedded in the Bluff Body,” *Micromachines (Basel).*, vol. 12, no. 6, p. 626, May 2021, doi: 10.3390/mi12060626.

[44] G. Hu, J. Wang, and L. Tang, “A comb-like beam based piezoelectric system for galloping energy harvesting,” *Mech. Syst. Signal Process.*, vol. 150, Mar. 2021, doi: 10.1016/j.ymssp.2020.107301.

[45] G. R. S. Assi and P. W. Bearman, “Transverse galloping of circular cylinders fitted with solid and slotted splitter plates,” *J. Fluids Struct.*, vol. 54, pp. 263–280, Apr. 2015, doi: 10.1016/j.jfluidstructs.2014.11.005.

[46] A. Bibo and M. F. Daqaq, “On the optimal performance and universal design curves of galloping energy harvesters,” *Appl. Phys. Lett.*, vol. 104, no. 2, Jan. 2014, doi: 10.1063/1.4861599.